

## FULL ARTICLE

# Photonic crystal enhanced fluorescence immunoassay on diatom biosilica

Kenneth Squire<sup>1†</sup> | Xianming Kong<sup>1,2\*†</sup> | Paul LeDuff<sup>3</sup> | Gregory L. Rorrer<sup>3</sup> | Alan X. Wang<sup>1\*</sup> 

<sup>1</sup>School of Electrical Engineering and Computer Science, Oregon State University, Corvallis, Oregon

<sup>2</sup>College of Chemistry, Chemical Engineering and Environment Engineering, Liaoning Shihua University, Fushun, Liaoning, China

<sup>3</sup>School of Chemical, Biological & Environmental Engineering, Oregon State University, Corvallis, Oregon

## \*Correspondence

Xianming Kong, College of Chemistry, Chemical Engineering and Environment Engineering, Liaoning Shihua University, Dandong Road 1, Fushun, Liaoning 113001, China.

Email: xmkong@lnpu.edu.cn

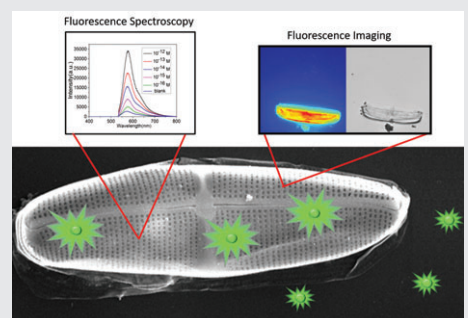
Alan X. Wang, School of Electrical Engineering and Computer Science, Oregon State University, 1148 Kelley Engineering Center, Corvallis, OR 97331.

Email: wang@eecs.oregonstate.edu

## Funding information

Directorate for Engineering, Grant/Award Number: 1701329; National Institute of Biomedical Imaging and Bioengineering, Grant/Award Number: R03EB018893; National Institute of Food and Agriculture, Grant/Award Number: 3017-67021-26606; National Institute on Drug Abuse, Grant/Award Number: 1R21DA0437131

Fluorescence biosensing is one of the most established biosensing methods, particularly fluorescence spectroscopy and microscopy. These are two highly sensitive techniques but require high-grade electronics and optics to achieve the desired sensitivity. Efforts have been made to implement these methods using consumer grade electronics and simple optical setups for



applications such as point-of-care diagnostics, but the sensitivity inherently suffers. Sensing substrates, capable of enhancing fluorescence are thus needed to achieve high sensitivity for such applications. In this paper, we demonstrate a photonic crystal-enhanced fluorescence immunoassay biosensor using diatom biosilica, which consists of silica frustules with sub-100 nm periodic pores. Utilizing the enhanced local optical field, the Purcell effect and increased surface area from the diatom photonic crystals, we create ultrasensitive immunoassay biosensors that can significantly enhance fluorescence spectroscopy as well as fluorescence imaging. Using standard antibody-antigen-labeled antibody immunoassay protocol, we experimentally achieved 100× and 10× better detection limit with fluorescence spectroscopy and fluorescence imaging respectively. The limit of detection of the mouse IgG goes down to  $10^{-16}$  M (14 fg/mL) and  $10^{-15}$  M (140 fg/mL) for the two respective detection modalities, virtually sensing a single mouse IgG molecule on each diatom frustule. The effectively enhanced fluorescence imaging in conjunction with the simple hot-spot counting analysis method used in this paper proves the great potential of diatom fluorescence immunoassay for point-of-care biosensing.

## KEYWORDS

biosensor, diatom, fluorescence imaging, fluorescence spectroscopy, immunoassay, photonic crystal enhanced fluorescence

## 1 | INTRODUCTION

Fluorescence biosensors have found applications in a broad range of fields because of their capability for extremely high

sensitivity, multiplex detection, and to cause little or no damage to the sample [1–4]. Two common modalities of fluorescence biosensing are fluorescence spectroscopy and fluorescence microscopy. Fluorescence spectroscopy is a highly sensitive detection modality and very well established. It is performed by exciting a sample with a light

<sup>†</sup>Both of these authors contributed equally.

source and measuring the emitted fluorescence signals that are inherent to the target, or a fluorescent tag, using a spectrometer. The fluorescence intensity is proportional to the amount of target molecules and based on the profile and intensity of the spectra, detection and quantification can be performed [5–8]. Fluorescence microscopy is one of the most widely used biosensing mechanism due to the high sensitivity and spatial resolution [9–14]. Fluorescence microscopy operates similarly to spectroscopy but rather than measuring the fluorescence spectra with a spectrometer, an imager is used such as a CCD or CMOS sensor array. Compared with fluorescence spectroscopy, which requires optical spectrometers, fluorescence microscopy can be performed with simple read-out equipment—only an optical filter and a camera. This, paired with the ease with which it can be performed, makes fluorescence microscopy a powerful biosensing technique. However, to achieve the desired high sensitivity with either modality, high-grade electronics and optics are required. This limits the applications of these sensing methods in point-of-care diagnostics. In order to achieve practical detection limits with consumer grade electronics, efforts have been made to implement various optical setups with additional complexity [15–17]. An alternative approach is the improvement of the sensing substrate. Many works have been published focusing on the creation of sensor substrates capable of enhancing measured fluorescence signals using a variety of structures including photonic crystals [18–21].

Photonic crystals are periodic dielectric materials that can be 1-, 2- or 3-dimensional. For fluorescence sensing, photonic crystal features are capable of enhancing the local optical field intensity [22, 23]. In addition, if a fluorophore is placed in proximity to a photonic crystal, it will experience enhanced emission due to the Purcell effect [24]. Such dual enhancement mechanisms, combined together, will lead to photonic crystal enhanced fluorescence detection that can achieve high levels of sensitivity without the need for high-grade electronics or optics. Fabricating rationally designed photonic crystal devices usually requires sophisticated fabrication equipment [25, 26] and relatively high cost, although the concerns have been relieved significantly by new techniques such as nano-imprinting [27]. Cell cultivation is a conventional bioprocess that can provide an alternative approach for fabricating nanoscale photonic structures with low cost and less complexity. Diatoms are unicellular marine organisms that have porous biosilica cell walls with dimensions on the order of 10 microns. The porous nature of the diatom frustule gives it roughly 11× more surface area than the glass surface (see File S1, Supporting Information) while the two-dimensional periodic nanosized pores endow it with hierarchical nanoscale photonic crystal features [28, 29]. We have previously shown the evaporation-based ability of diatoms to concentrate analytes [30]. Our research group has also previously shown that diatoms are capable of enhancing

the electromagnetic field on its surface for SERS sensing [22, 23, 30, 31] and an ultra-sensitive SERS immunoassay has been developed, achieving a detection limit of mouse IgG down to 10 pg/mL [32].

In this paper, we develop a novel photonic crystal enhanced fluorescence immunoassay biosensor on diatom biosilica. We demonstrate enhancement in fluorescence spectroscopy signals of more than 100× in comparison to an equivalent non-diatom based biosensor allowing detection down to 100 aM (14 fg/mL). Utilizing fluorescence microscopy, we achieved a 10× enhancement of the limit of detection compared to non-diatom sensors and a 27-2700× enhancement in a hot-spot counting method, achieving detection down to 1 fM (140 fg/mL). The fluorescence immunoassay in this work improved the detection limit by 100-1000× compared with our previous SERS immunoassay, allowing for single molecule mouse IgG detection on diatom frustules. The effectively enhanced fluorescence imaging, coupled with a simple hot-spot counting analysis method used in this paper proves the ability of diatom fluorescence immunoassay for highly sensitive biosensors and the great potential for point-of-care diagnostics.

## 2 | EXPERIMENTAL

### 2.1 | Simulation

Two mechanisms are capable of enhancing the fluorescence signal of a fluorophore on diatom. The first mechanism enhances the excitation while the second intensifies the emission. The enhanced excitation comes from a strengthened local optical field on the surface of the photonic crystal. Incident light induces resonant modes within the structure that, in turn, increase the optical field on the surface which in turn causes greater excitation of the fluorophore [33, 34]. This has been investigated previously by our research group and the diatom structure has been theoretically shown capable of enhancing the excitation intensity by 10× [30]. The enhanced emission comes from an increased emission rate due to the Purcell effect [24, 35]. When a fluorophore is placed on a photonic crystal slab, the density of optical states increases, resulting in a greater emission rate from the fluorophore.

To explore the enhanced emission of fluorophores on diatom surface, we performed a finite-difference time-domain (FDTD) analysis. The structure is modeled after the *Pinnularia sp.* diatom which we used in our experiments. The model is comprised of a silica slab with periodic air holes to simulate the pores. The dimensions of the simulated structure were chosen according to dimensions found from the SEM image of diatoms [30]. The pores are 160 nm in diameter with nanoscale features at the bottom. They are two-dimensionally periodic with a period of 300 nm along the major and minor axes of the structure. These dimensions are shown in Figure 1A and B. The structure is 15 × 5 μm

which is similar to the actual size of the diatoms. This structure was used to simulate the Purcell effect of the diatom frustule.

As the Purcell effect is related to the emission of a fluorophore, a single electric dipole representing the emission of a previously excited fluorophore was used to simulate the Purcell effect. This dipole was placed at various points as shown in Figure 1C to excite electric fields in the nano-structure. The Purcell factor was calculated from the dipole source as the ratio of the power emitted in the photonic crystal environment compared to that emitted in a homogenous material. The emission wavelength of the dipole was swept from 400-700 nm in order to acquire the structure's Purcell effect. In Figure 1D the Purcell factor is plotted with respect to the wavelength. The shaded region represents the emission region of R6G which is the fluorescence tag used in our experiment and represents the expected enhancement in our experiment. The simulation shows that when the fluorophore is near the nanopore, the power emitted by a fluorophore is enhanced by 1.5 to 3 $\times$  across our region of interest due to the Purcell effect. Overall, the fluorophores inside the nanopores (B and C in Figure 1C) will experience stronger Purcell effect compared with that (A in Figure 1C) on the surface of the frustule.

For fluorescence biosensing, it is equally critical to efficiently collect the fluorescence signals. To address this concern, the far-field radiation patterns of a dipole on diatom and on glass were simulated. Simulating the radiation pattern of a fluorophore on diatom, as shown in Figure 2A, shows that there are a few strongly focused radiation directions at large angles of 70°-80°, which is quite surprising. The reason is that a significant amount of the fluorescence emission from the fluorophore is coupled into the slab waveguide and emitted from the edge, which contributed to the large angle radiation. In reality, however, the surface roughness and curvature of the frustule

(see Figure 4 for details) will scatter these slab modes and homogenize the radiation in the solid angle. Nevertheless, we still investigated the radiation pattern within a 50° cone. Our fluorescence spectroscopy measurements were done using an objective lens with a numerical aperture of 0.75, which has a corresponding 50° half angle of acceptance directly above and normal to the sample. To investigate the collection efficiency of fluorescence light, the far-field radiation patterns are shown on diatom and glass in Figure 2B and C respectively. As can be seen, the emission from the fluorophore on diatom is more intense than that found on glass and by averaging the collected intensity in both instances. The enhancement by diatom is calculated to be 1.7 $\times$ . When combined with the enhanced excitation, we expect the total measured fluorescence enhancement from diatom to be on the order of 10 $\times$ . This analysis applies to single molecule or a few molecule sensing. If a large number of randomly distributed fluorophores emit light with random polarization, corresponding to the biosensing of high-concentration analyte, we may not observe any dependence of the radiation on the direction. The fluorescence emission from both diatom and glass will be relatively homogenous.

## 2.2 | Materials and reagents

Anhydrous ethanol (EtOH) was purchased from Macron. The bovine serum albumin (BSA), aminopropyl-triethoxysilane (APTES), glutaraldehyde (GA), antibody (goat anti-mouse IgG), antigen (mouse IgG) and antibody labeled with Rhodamine 6G (R6G) (goat anti-mouse IgG-R6G) were obtained from Sigma-Aldrich. The chemical reagents used were of analytical grade. Water used in all experiments was deionized and further purified by a Millipore Synergy UV Unit to a resistivity of  $\sim$ 18.2 M $\Omega$  cm.

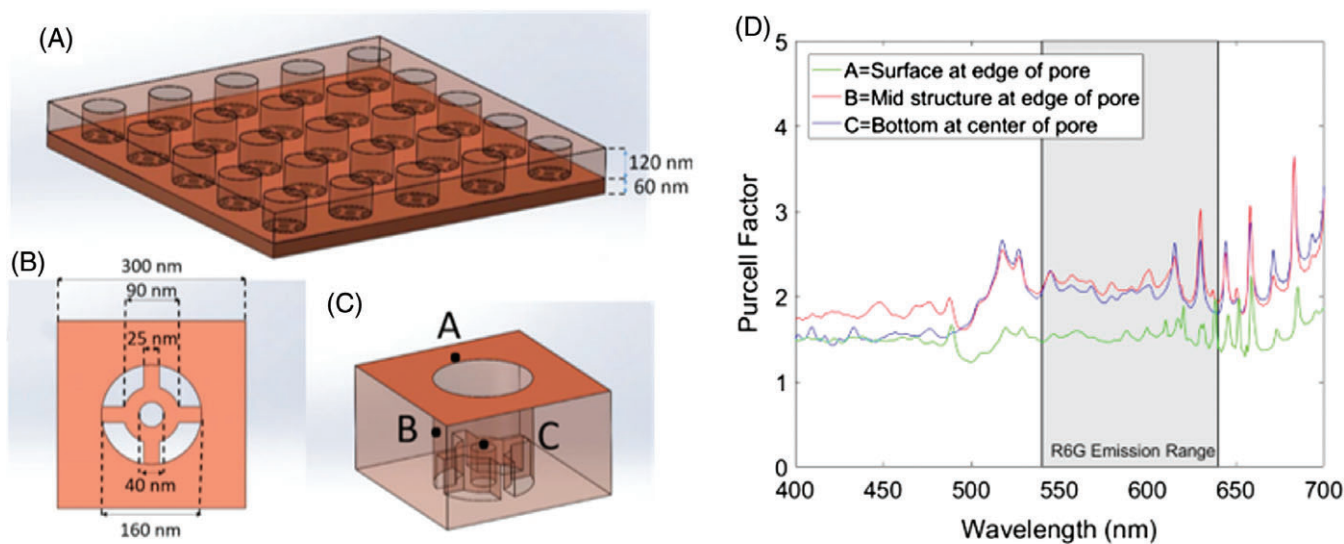


**FIGURE 1** (A) Simulated slab structure with 5  $\times$  5 array of nanopores; (B) enlarged view of the nanopore with geometric parameters; (C) placement of fluorophores in diatom frustules; (D) the Purcell effect simulation results at the three points within a unit cell as a function of the wavelength

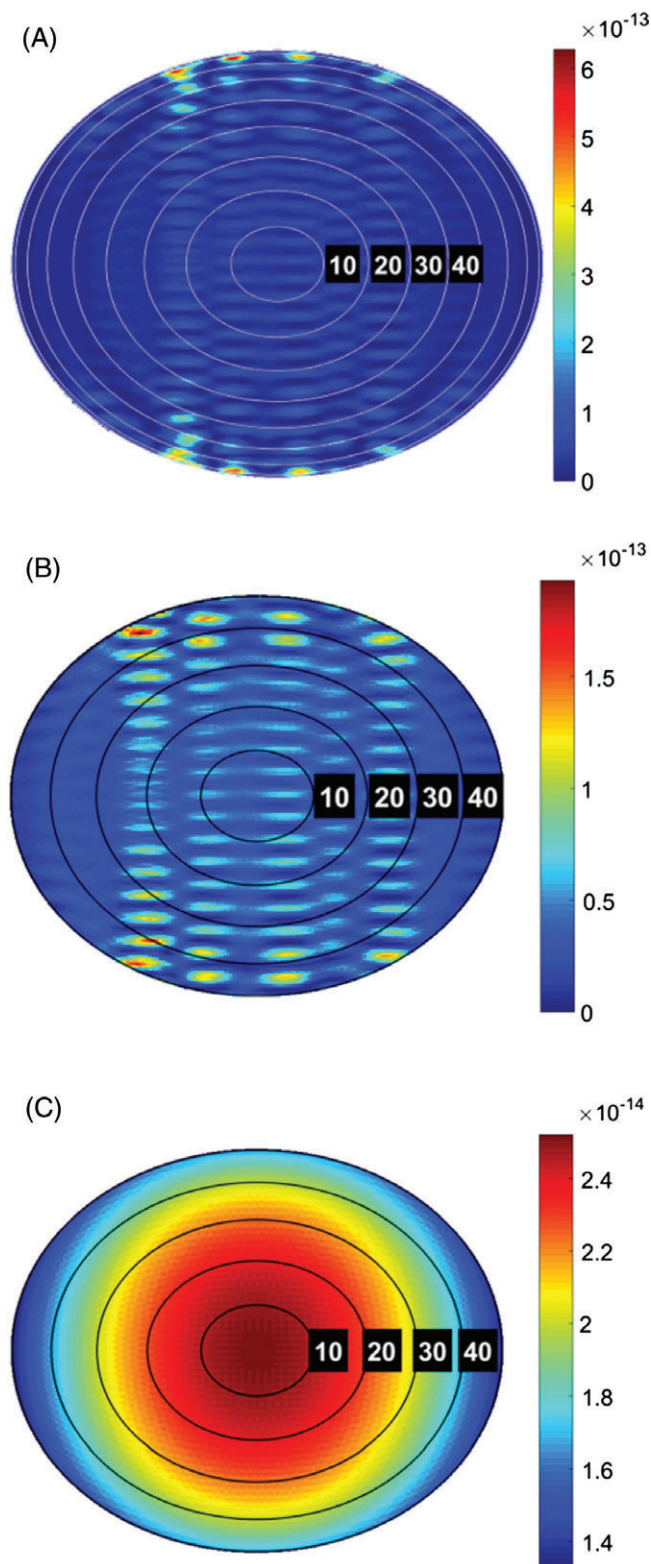


**FIGURE 2** Far-field radiation pattern of fluorophore on diatom (A), and radiation pattern inside the  $50^\circ$  solid angle on diatom (B) and glass (C)

### 2.3 | Preparation of diatom biosilica

Diatom (*Pinnularia sp.*) biosilica were prepared according to the method previously reported with minor modification [30]. Briefly, diatoms were cultured in a container for one week. The diatom suspension was concentrated 10 $\times$  through centrifuging and dispersed in sterile filtered artificial seawater,

and filtered with 20  $\mu\text{m}$  mesh to separate cells. The diatom cell density was adjusted to  $0.1 \times 10^5$  cells/mL for seeding. A coverslip was placed into a petri dish separately, and 15 mL of diatom cell suspension was cast onto the glass slides, and incubated in a humidifier chamber for 1 hour to deposit the cells on the coverslip surface. Then the coverslip with diatoms was put into a new petri dish, kept in a humidifier for 24 hours and immersed in 70% EtOH for 4 hours, and soaked in pure EtOH for 4 more hours. The diatoms were dried in air and treated in a UV ozone cleaner at  $90^\circ\text{C}$  for one day. After that, the diatom substrate was ready for use.

### 2.4 | Preparation of diatom fluorescence immunoassay

The diatom biosensor was prepared as shown in Figure 3. The diatom substrate was incubated in 15 mL of 0.05% APTES in EtOH (v/v) for 6 hours at room conditions followed by washing with acetone and EtOH and drying with nitrogen gas. After that, the aminated diatom substrate was immersed in 15 mL of 2% (v/v) glutaraldehyde (GA) in phosphate buffer saline (PBS) for 2 hours. The GA-modified diatom was washed thoroughly with double-distilled water three times to remove excess GA and again dried with nitrogen. The GA-activated surface was then reacted with 0.1 mg/mL of goat anti-mouse IgG in PBS buffer by drop casting 1  $\mu\text{L}$  onto various points on the sensor and leaving at  $4^\circ\text{C}$  for 6 hours to get an antibody layer followed by another rinsing with PBS and water and drying with nitrogen. After this step, the sample was submerged in 1 mg/mL of BSA in PBS and left at room temperature for 6 hours to block the remaining GA-active surface to reduce the non-specific binding of the immunoassay. The antibody immobilized diatom substrates were rinsed with PBS and water, dried with nitrogen, and stored at  $4^\circ\text{C}$  for future immunoassay procedures.

The immunoassay procedure is similar to a standard sandwich protocol of the enzyme-linked immunosorbent assay, as shown in Figure 3. Briefly, 1  $\mu\text{L}$  of antigen (mouse IgG) at different concentrations was pipetted onto spots corresponding with immobilized goat anti-mouse IgG antibody on the diatom substrate. After 2 hours of immune recognition at room temperature, the substrate was rinsed with PBS buffer and water followed by a drying step with nitrogen. Next, 1  $\mu\text{L}$  of goat-anti-mouse IgG labeled with R6G was pipetted onto the same spots of the substrate and kept at  $4^\circ\text{C}$  for 4 hours and washed thoroughly with PBS buffer and water. The sensor was dried using nitrogen gas and was then ready for fluorescence measurements.

## 3 | RESULTS AND DISCUSSION

### 3.1 | Diatom-enhanced fluorescence spectroscopy

The morphology of the diatom photonic crystal biosilica was characterized by scanning electron microscopy (SEM). The

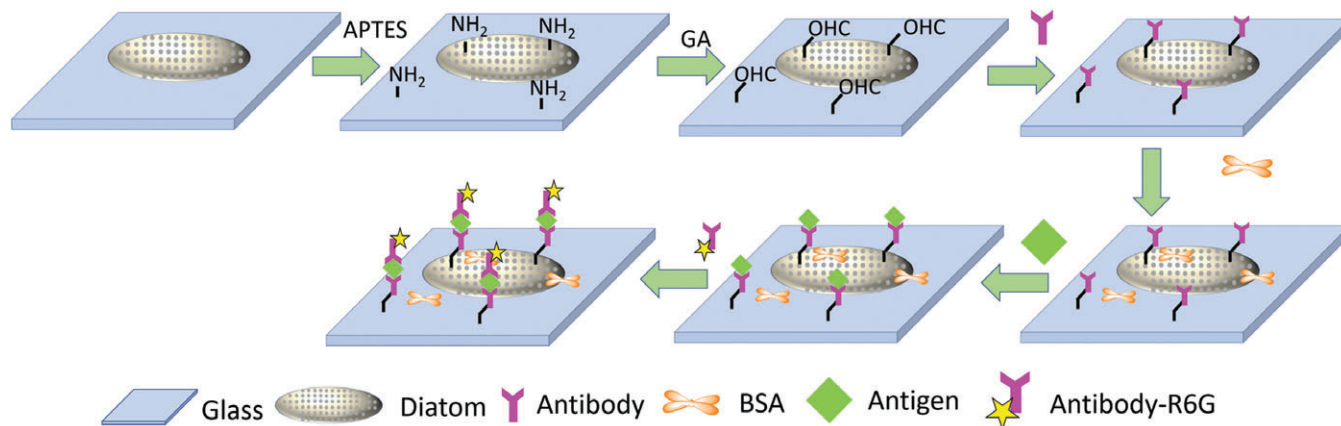


**FIGURE 3** Schematic illustration of the fluorescence microscopy immunoassay sensing on diatom photonic crystal biosilica

SEM images of diatom are shown in Figure 4A and B. The semi-ellipsoidal cell dimension of diatom is around  $25\ \mu\text{m}$  along the major axis,  $8\ \mu\text{m}$  along the minor axis. The diatom biosilica consists of periodic two-dimensional nanopores (Figure 4B) with a periodicity of  $300\ \text{nm}$ . At the floor of the pores, additional nanofeatures are present. The fluorescence enhancement effect of the diatom photonic biosilica was investigated using Rhodamine 6G (R6G) as the typical probe molecule due to its strong fluorescence feature. First,  $1\ \mu\text{L}$  of R6G aqueous solution was cast onto the glass-diatom substrate. After drying in air, the fluorescence image of the glass-diatom substrate was obtained under a fluorescence microscope with  $532\ \text{nm}$  laser as the excitation light. Additional information about the fluorescence spectra acquisition is given in the File S1, Supporting Information. As shown in Figure 4C, the orange color from the diatom photonic biosilica is brighter than that from the glass slide. The contrast between the diatom and glass was attributed to the photonic crystal enhancement effect from diatom frustules. The fluorescence enhancement effect of diatom photonic biosilica was further verified by fluorescence spectra as shown in Figure 4D. The sample used to collect the fluorescence spectra was the same one that was used for fluorescence image acquisition in Figure 4C. The intensity of the fluorescence spectra of R6G from diatom photonic biosilica are almost  $10\times$  that from the glass slide, which is in accordance with the fluorescence imaging result.

The target antigen, mouse IgG, varying from  $1\ \text{pM}$  to  $0.1\ \text{fM}$  was applied to the sensor as outlined in the previously stated immunoassay protocol section. Figure 5A shows the fluorescence spectra of the R6G-labeled immuno-complex on diatom frustules with different antigen concentrations. It can be observed that the intensity of the peak decreases gradually with the decrease of antigen concentrations. When the concentration of mouse IgG decreases to  $0.1\ \text{fM}$ , the fluorescence intensity at  $575\ \text{nm}$  is still easily observed compared to the control sample. In contrast, on the glass slides, when the concentration of mouse IgG decreases

to  $10\ \text{fM}$ , it is difficult to distinguish the fluorescence signal of R6G from the control as shown in Figure 5B. This demonstrates a  $100\times$  enhancement from our sensor. The superior performance can be attributed to the photonic crystal effect of the diatom frustules, from both enhanced excitation and the Purcell effect. It is interesting to point out that there is not any trace of Purcell effect modulation as the simulation results in Figure 1D in the experimental spectra. This is because the diatom structure is not perfectly periodic over a long range as the simulation model. Therefore, the local Purcell factor varies from diatom to diatom and even across the diatom frustule. This creates an averaging effect of the Purcell effect which results in the absence of this modulation.

### 3.2 | Fluorescence imaging average intensity analysis

To further explore the capabilities of our sensor, optical and fluorescence images were taken of diatoms using a fluorescence microscope. Varying concentrations of antigen were imaged and it is observed that the fluorescence intensity decreases as the antigen concentration decreases as shown in Figure 6. The average fluorescence intensity was calculated and used to determine the presence of the analyte. The methodology for calculating the average intensity on diatom and glass is outlined in the File S1, Supplemental Information.

The fluorescence intensity on diatom and on glass was analyzed and the average at each concentration, along with error bars of the standard deviation, was plotted with respect to concentration as shown in Figure 7A. The noise floor was defined as  $3\times$  the signal-to-noise ratio (SNR). The SNR was defined as shown in Eq. (1) below where  $I_{\text{signal}}$  is the average fluorescence intensity for a given concentration and  $I_{\text{blank}}$  is the average fluorescence when there is no antigen present.

$$\text{SNR} = \frac{I_{\text{signal}}}{I_{\text{blank}}} \quad (1)$$

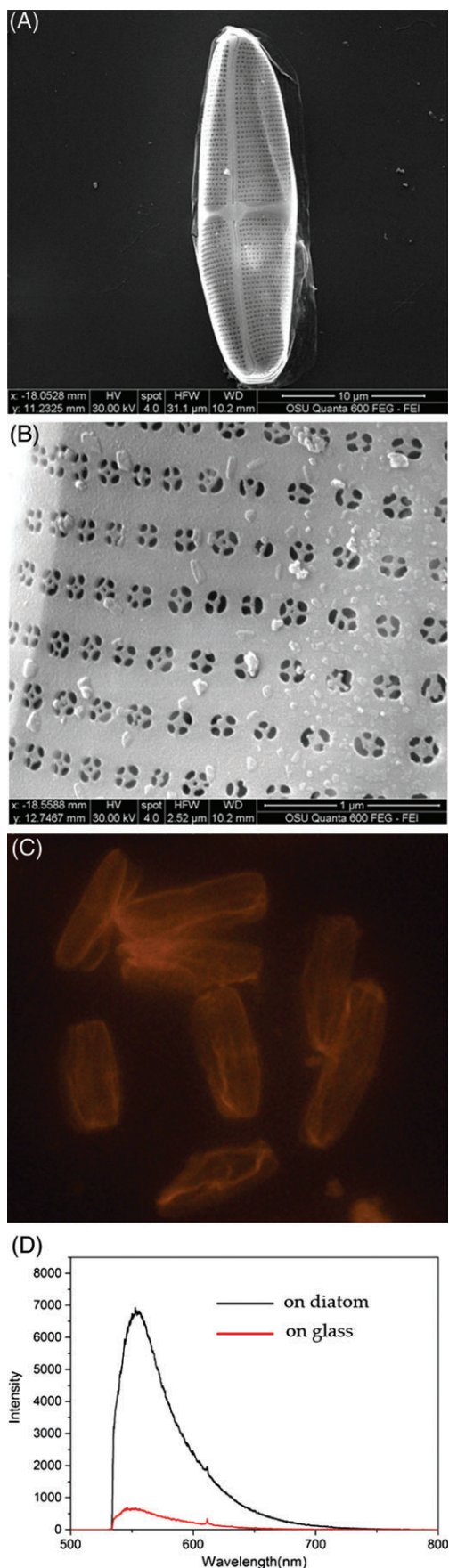


**FIGURE 4** SEM images of (A) an overview of a single diatom frustule, (B) primary pores on a frustule, (C) fluorescence image of 1  $\mu\text{L}$  of R6G ( $10^{-6}$  M) dropped onto the glass-diatom substrate, (D) fluorescence spectra of 1  $\mu\text{L}$  of R6G ( $10^{-6}$  M) solution dropped onto the glass-diatom substrate

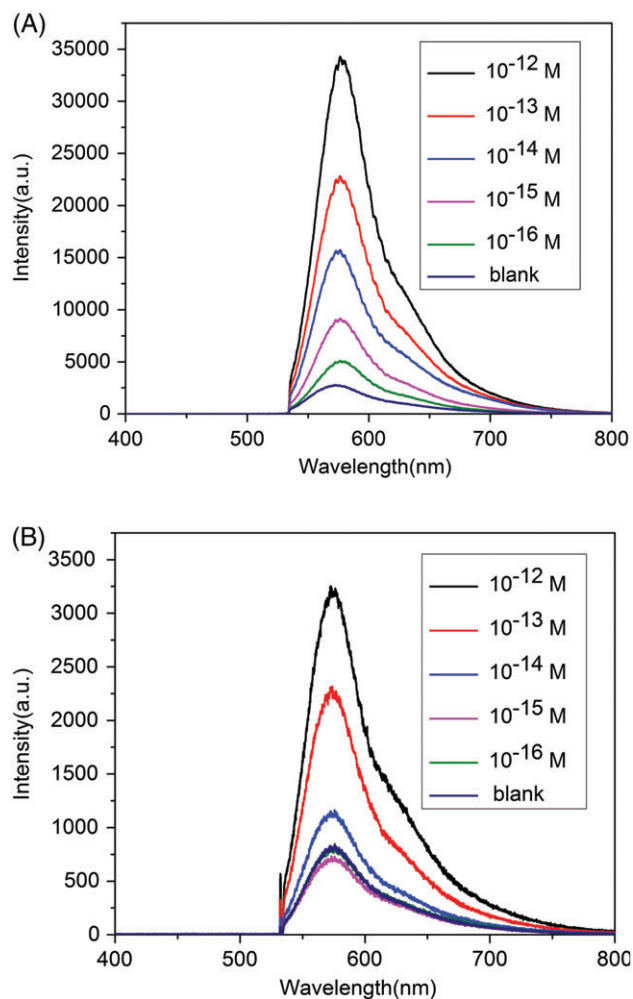


**FIGURE 5** Fluorescence spectra on diatom (A) and glass (B) for different concentrations of IgG

The SNR with respect to concentration on diatom and on glass are plotted in Figure 7B. The enhancement factor due to diatom was calculated according to Eq. (2) where  $I_{\text{avg,d}}$  is the average fluorescent intensity on diatom and  $I_{\text{avg,g}}$  is the average intensity on glass. The enhancement factor was plotted with respect to concentration in Figure 7C.

$$EF = \frac{I_{\text{avg,d}}}{I_{\text{avg,g}}} \quad (2)$$

Using this methodology, a limit of detection of 10 fM was achieved as shown in Figure 7A. A maximum SNR of 50 was achieved on diatom and an enhancement as high as 6 $\times$  from diatom was achieved at antigen concentration of  $10^{-9}$  M. The reproducibility of our sensors is shown in the File S1, Supporting Information. As the concentration decreases, so do the SNRs, as well as the enhancement factor from diatom. This can be easily understood. At higher concentrations, the analyte is abundant and is considered to be uniformly dispersed across the sample. However, at lower concentrations, such as

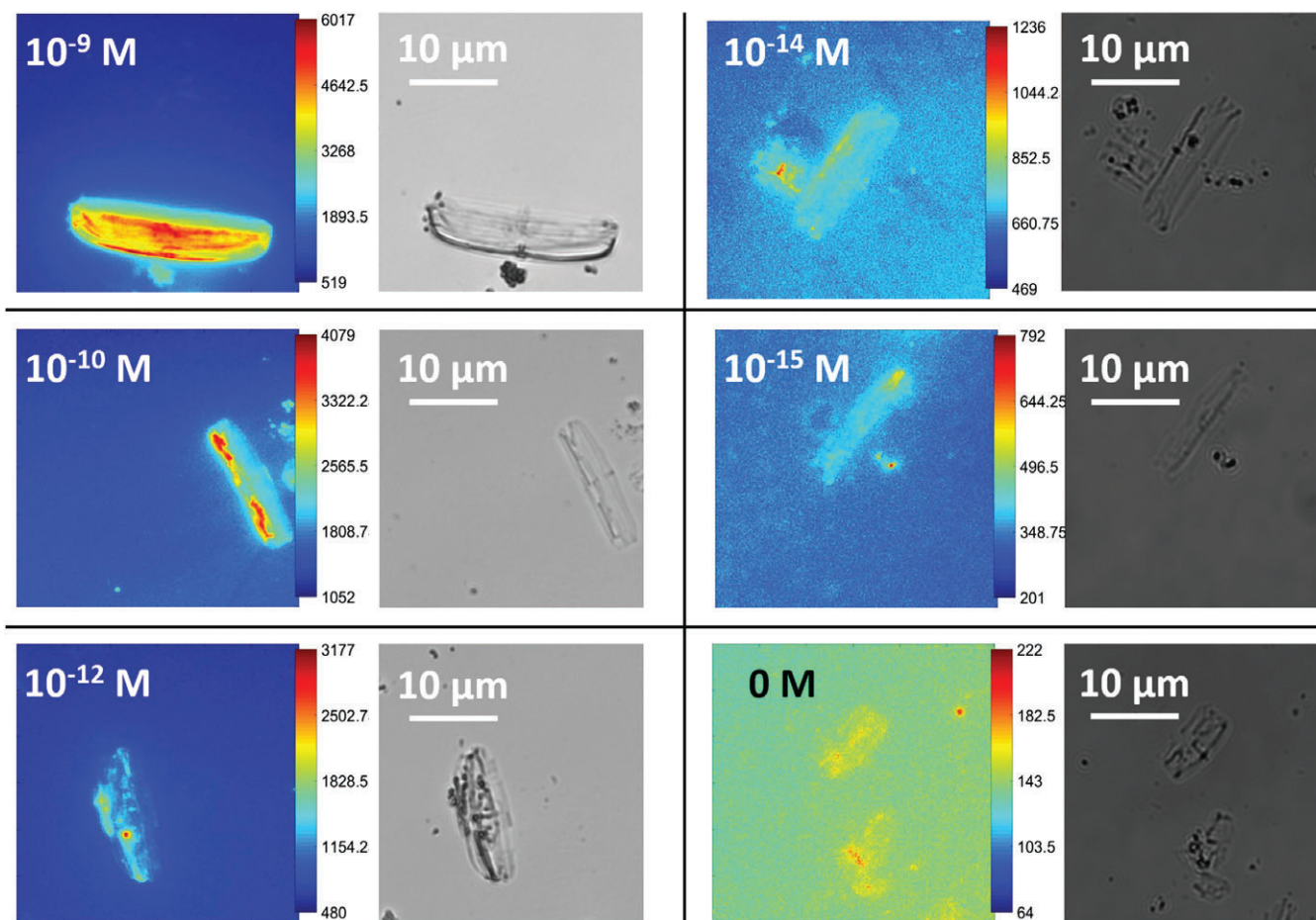


FIGURE 6 Fluorescence and optical images of diatoms at varying concentrations of R6G-tagged mouse IgG

1 fM, the density of fluorophores is closer to single molecule levels. At this concentration, the molecules are no longer uniformly dispersed and by averaging the whole diatom, the enhancement factor of the fluorescence signals is diluted.

### 3.3 | Fluorescence imaging hot-spot analysis

As a more accurate method, a hot-spot counting analysis was performed rather than analyzing the average intensity. A hot-spot was defined as a pixel whose intensity is three times the noise floor. Counting the number of hot-spots, the hot-spot occupation ratio is calculated on the glass and the diatom by using Eq. (3) where  $R$  is the occupation the number of pixels that are hot-spots.

$$R = \frac{N_{hs}}{N_p}. \quad (3)$$

Performing this hot-spot counting analysis at several concentrations, we pushed our limit of detection down to 1 fM, achieving detection an order of magnitude lower than the large area averaging technique. As is shown in Figure 8, a massive enhancement due to the diatom was achieved

ranging from 27 $\times$  up to 2700 $\times$ . The mechanics of this enhancement is discussed in depth in the File S1, Supporting Information. Due to the ultra-low concentrations, the non-uniformity of the analyte leads to large variations in hot-spot occupation ratio. An image may contain a couple of fluorophores or there may be none. For our measurements, diatoms with fluorescent signals were imaged and then compared to their surrounding glass. Because diatoms exhibiting fluorescence were selectively imaged, the variation in hot-spot occupation ratio on diatom is relatively small. However, the hot-spot occupation ratio on glass surrounding the diatom varies largely between samples as can be seen in Figure 8. This large variation on glass is caused by the non-uniformity of the analyte and is responsible for the wide range of enhancement factors. Nevertheless, the enhancement factor of more than 20 $\times$  is guaranteed for single-molecule detection. Requiring at least a hot-spot occupation ratio of at least 1% for detection, we achieve detection limits of 1 fM on diatom and 10 fM on glass. This 10 $\times$  improvement to the limit of detection is attributed to the enhancements from diatom, thus proving the merit of diatom-based biosensors for enhanced fluorescence.

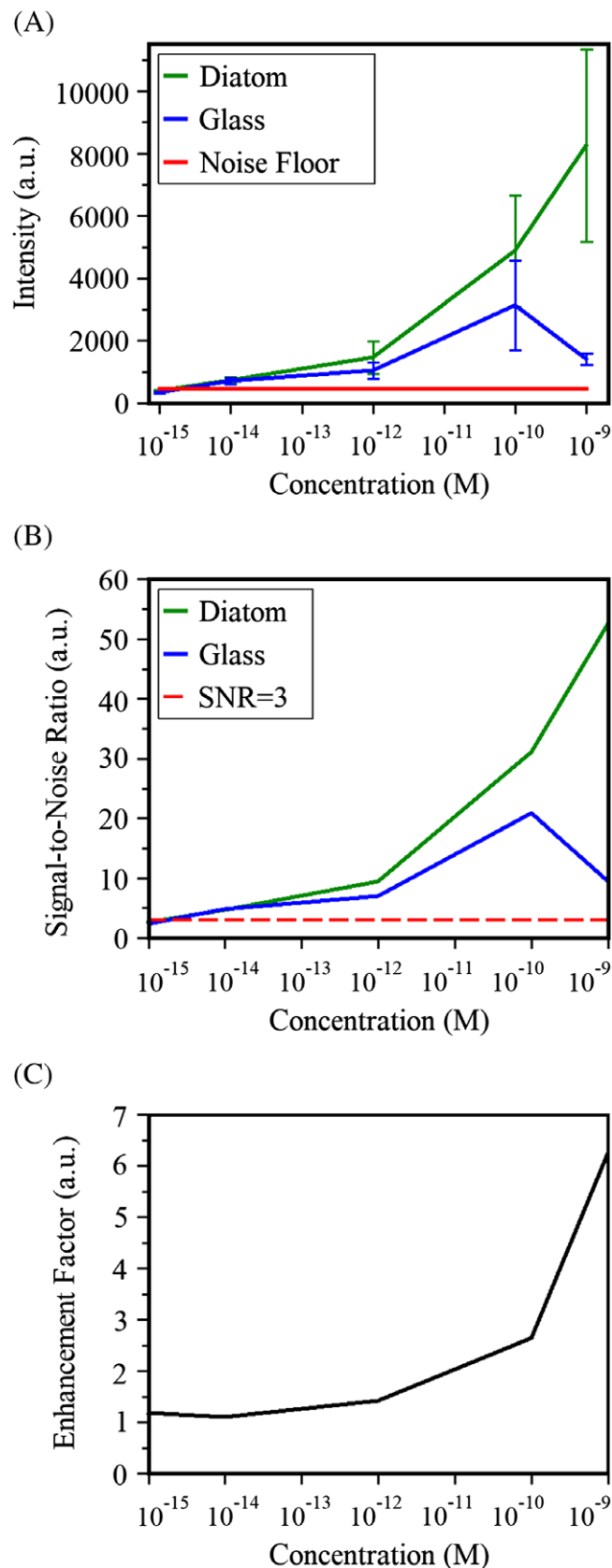


**FIGURE 7** Average fluorescence on diatom and glass with error bars, along with the noise floor (A). The SNR is shown for diatom and glass with respect to concentration with a line representing SNR = 3 (B). The enhancement factor is also calculated at each concentration (C)

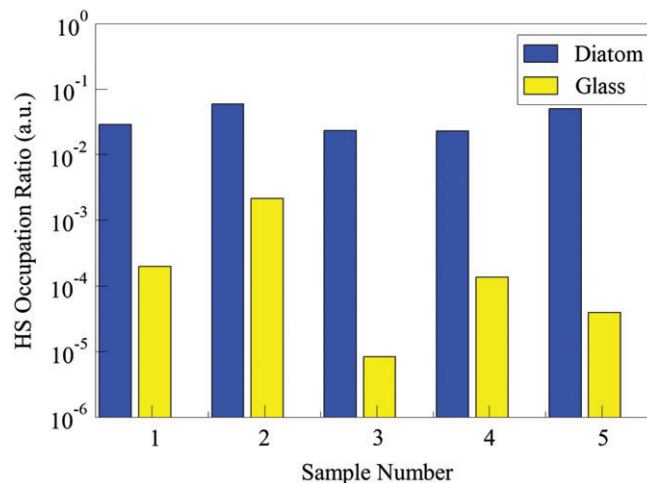


**FIGURE 8** The hot-spot occupation ratio on diatom and glass plotted on a log scale for several samples with analyte concentration at  $10^{-15}$  M

#### 4 | CONCLUSION

In summary, we demonstrated a photonic crystal enhanced fluorescence microscopy including both fluorescence spectroscopy and fluorescence imaging on diatom biosilica. The porous nanostructures and the photonic crystal features of diatoms are combined in a synergistic way to achieve ultra-sensitive immunoassay detection. We experimentally achieved 100× and 10× better detection limit with fluorescence spectroscopy and fluorescence imaging respectively. The limit of detection of the mouse IgG goes down to  $10^{-16}$  M (14 fg/mL) and  $10^{-15}$  M (140 fg/mL) for the two respective detection modalities, virtually sensing a single mouse IgG molecule on each diatom frustule. The effectively enhanced fluorescence imaging, in conjunction with the simple hot-spot counting analysis method used in this paper, proves the great ability of diatom fluorescence immunoassay to enhance fluorescence and achieve high sensitivity. This sensor is ideal for point-of-care fluorescence microscopy diagnostics, particularly cell phone-based diagnostics. Cell phone-based biosensors have a lot of attention in recent years [15–17, 36, 37] and the advantages of such a system are obvious, particularly in rural and low-income areas as well as developing nations. We expect that the diatom photonic crystal enhanced fluorescence immunoassay can be used as a versatile device for cell phone-based POC diagnosis in rural and underdeveloped areas and we will investigate this in our future work.

#### ACKNOWLEDGMENTS

The authors would like to acknowledge the support from the National Institutes of Health under Grant

No. 1R21DA0437131 and R03EB018893, the National Science Foundation under Grant No. 1701329, and the United States Department of Agriculture under Grant No. 2017-67021-26606. The authors also acknowledge the support from Marine Polymer Technologies, Inc. The group would also like to thank Mr. Bo Wu and Dr Li-Jing Cheng for their assistance in measuring the fluorescence spectroscopy.

## AUTHOR BIOGRAPHIES

Please see Supporting Information online.

## ORCID

Alan X. Wang  <http://orcid.org/0000-0002-0553-498X>

## REFERENCES

- [1] S. Weiss, *Science* **1999**, 283, 1676.
- [2] J. Lakowicz, *Topics in Fluorescence Spectroscopy*, Plenum Press, New York, NY **1994**, p. 1.
- [3] J. Pickup, F. Hussain, N. Evans, O. Rolinski, D. Birch, *Biosens. Bioelectron.* **2005**, 20, 2555.
- [4] F. Luo, L. Zheng, S. Chen, Q. Cai, Z. Lin, B. Qiu, G. Chen, *Chem. Commun.* **2012**, 48, 6387.
- [5] E. Sikorska, A. Gliszczynska-Swiglo, I. Khmelinskii, M. Sikorski, *J. Agric. Food Chem.* **2005**, 53, 6988.
- [6] L. Yi, H. Li, L. Sun, L. Liu, C. Zhang, Z. Xi, *Angew. Chem. Int. Ed.* **2009**, 48, 4034.
- [7] H. Jo, J. Her, C. Ban, *Biosens. Bioelectron.* **2015**, 71, 129.
- [8] J. Zhang, L. Wang, H. Zhang, F. Boey, S. Song, C. Fan, *Small* **2010**, 6, 201.
- [9] A. Sheahan, T. Sekar, K. Chen, R. Paulmurugan, T. Massoud, *J. Mol. Med.* **2016**, 94, 799.
- [10] X. Lu, P. Nicovich, K. Gaus, J. Gooding, *Biosens. Bioelectron.* **2017**, 93, 1.
- [11] E. Stelzer, *Nat. Methods* **2015**, 12, 23.
- [12] H. Deschout, F. Zancchi, M. Mlodzianoski, A. Diaspro, J. Bewersdorf, S. Hess, K. Braeckmans, *Nat. Methods* **2014**, 11, 253.
- [13] A. Kuroda, M. Alexandrov, T. Nishimura, T. Ishida, *Biotechnol. J.* **2016**, 11, 757.
- [14] X. Gao, C. Ding, A. Zhu, Y. Tian, *Anal. Chem.* **2014**, 86, 7071.
- [15] D. Breslauer, R. Maamari, N. Switz, W. Lam, D. Fletcher, *PLoS One* **2009**, 4, e6320.
- [16] H. Zhu, O. Yaglidere, T. W. Su, D. Tseng, A. Ozcan, *Lab. Chip* **2011**, 11, 315.
- [17] A. Cosckun, R. Nagi, K. Sadeghi, S. Phillips, A. Ozcan, *Lab. Chip* **2013**, 13, 4231.
- [18] N. Ganesh, I. Block, P. Mathias, W. Zhang, E. Chow, V. Malyarchuk, B. Cunningham, *Opt. Express* **2008**, 16, 21626.
- [19] M. Bauch, K. Toma, M. Toma, Q. Zhang, J. Dostalek, *Plasmonics* **2014**, 9, 781.
- [20] D. Gallegos, K. D. Long, H. Yu, P. P. Clark, Y. Lin, S. George, P. Nath, B. T. Cunningham, *Lab. Chip* **2013**, 13, 2124.
- [21] S. Dutta, K. Saikia, P. Nath, *RSC Adv.* **2016**, 6, 21871.
- [22] F. Ren, J. Campbell, X. Wang, G. L. Rorrer, A. X. Wang, *Opt. Express* **2013**, 21, 15308.
- [23] X. Kong, Y. Xi, P. Le Duff, X. Chong, E. Li, F. Ren, G. L. Rorrer, A. X. Wang, *Biosens. Bioelectron.* **2017**, 88, 63.
- [24] E. Purcell, *Phys. Rev.* **1946**, 69, 681.
- [25] C. -C. Cheng, A. Scherer, *J. Vac. Sci. Technol.* **1995**, 13, 2696.
- [26] M. Campbell, D. N. Sharp, M. T. Harrison, R. G. Denning, A. J. Turberfield, *Nature* **2000**, 404, 53.
- [27] A. Pokhriyal, M. Lu, V. Chaudhery, C. Huang, S. Schultz, B. Cunningham, *Opt. Express* **2010**, 18, 24793.
- [28] H. Li, B. Jiang, X. Yang, M. Eastman, Y. Liu, L. Wang, J. Campbell, L. Lampert, R. K. Wang, G. L. Rorrer, *ACS Photonics* **2014**, 1, 477.
- [29] L. De Stefano, P. Maddalena, L. Moretti, I. Rea, I. Rendina, E. De Tommasi, V. Mocella, M. De Stefano, *Superlattices Microstruct* **2009**, 46, 84.
- [30] X. Kong, Y. Xi, P. LeDuff, E. Li, Y. Liu, L. -J. Cheng, G. L. Rorrer, H. Tan, A. X. Wang, *Nanoscale* **2016**, 8, 17285.
- [31] X. Kong, Q. Yu, E. Li, R. Wang, Q. Liu, A. X. Wang, *Materials* **2018**, 11, 539.
- [32] J. Yang, L. Zhen, F. Ren, J. Campbell, G. L. Rorrer, A. X. Wang, *J. Biophotonics* **2015**, 8, 659.
- [33] N. Ganesh, W. Zhang, P. Mathias, E. Chow, J. Soares, V. Malyarchuk, A. Smith, B. Cunningham, *Nat. Nanotechnol.* **2007**, 2, 515.
- [34] Y. Hung, I. I. Smolyaninov, C. C. Davis, H. Wu, *Opt. Express* **2006**, 14, 10825.
- [35] S. V. Gaponenko, V. N. Bogomolov, E. P. Petrov, A. M. Kapitonov, D. A. Yarotsky, I. I. Kalosha, A. A. Eychmueller, A. L. Rogach, J. McGilp, U. Woggon, F. Gindele, *J. Lightwave Technol* **1999**, 17, 2128.
- [36] H. Yu, Y. Tan, B. Cunningham, *Anal. Chem.* **2014**, 86, 8805.
- [37] W. Chen, H. Yu, F. Sun, A. Ormob, R. Brisbin, A. Ganguli, V. Vemuri, P. Strzebonski, G. Cui, K. Allen, S. Desai, W. Lin, D. Nash, D. Hirschber, I. Brooks, R. Bashir, B. Cunningham, *Anal. Chem.* **2017**, 89, 11219.

## SUPPORTING INFORMATION

Additional supporting information may be found online in the Supporting Information section at the end of the article.

**File S1.** Supporting Information

**FIGURE S1** Peak fluorescence spectra intensity at 575 nm as a function of IgG concentration on diatom (A) and on glass (B)

**FIGURE S2** Linear fitting on diatom (A) and on glass (B)

**FIGURE S3** Average and SD of the fluorescence on diatom and glass showing the reproducibility of our diatom-based sensor

**FIGURE S4** The distribution of pixel fluorescent intensities on glass (A) and on diatom (B) with a shaded region represents the portion that are hot-spots

**Table S1** Correlation coefficient and linear fit parameters for diatom and glass

**How to cite this article:** Squire K, Kong X, LeDuff P, Rorrer GL, Wang AX. Photonic crystal enhanced fluorescence immunoassay on diatom biosilica. *J. Biophotonics*. 2018;e201800009. <https://doi.org/10.1002/jbio.201800009>